PHYSICAL REVIEW FLUIDS **9**, 053907 (2024)

Editors' Suggestion Featured in Physics

Longitudinal and azimuthal thermoacoustic modes in a pressurized annular combustor with bluff-body-stabilized methane-hydrogen flames

Byeonguk Ahn,* Håkon T. Nygård, and Nicholas A. Worth
Department of Energy and Process Engineering, Norwegian University of Science and Technology, 7491 Trondheim, Norway

Zhijian Yang and Larry K. B. Li
Department of Mechanical and Aerospace Engineering, The Hong Kong University of Science and Technology, Clear Water Bay, Hong Kong

(Received 19 October 2023; accepted 12 March 2024; published 10 May 2024)

In this experimental study on a methane-hydrogen fired laboratory-scale pressurized annular combustor, various steady and transient operating conditions were explored. Under steady operation, the thermoacoustic stability depended strongly on the equivalence ratio, but only weakly on the mass flow rate and hydrogen power fraction. During transient equivalence-ratio ramps, the predominant instability of the system switched between standing and spinning azimuthal modes. The ramping rate influenced the thermoacoustic amplitude during the switching, as well as the onset and decay of the different modes. The strong acoustic reflection at the choked outlet produced significant harmonic content during both steady and transient operation. Nonlinear time-series analysis and clustering algorithms showed that the Jensen-Shannon complexity and the permutation entropy could accurately classify the modal dynamics in an unsupervised manner. The classification revealed that standing azimuthal modes, with several preferred orientations, dominated under steady operation. The amplitude of the heat-release-rate (HRR) oscillations around the annulus depended on the mode orientation. The energy contribution from the harmonic components was isolated via bandpass filtering, revealing that the orientation of the first harmonic ($n = 2$) followed the fundamental mode, eliminating negligible HRR oscillation regions at the pressure node of the fundamental mode. By filtering out the higher-order harmonic content, intermittent switching between high-amplitude periodicity and low-amplitude chaos in the fundamental azimuthal mode was uncovered. Tools from dynamical systems theory confirmed the existence of chaos and demonstrated that the intermittency belongs to the type-II Pomeau-Manneville class. This study provides evidence of the type-II intermittency route to chaos in an annular combustor with longitudinal and azimuthal modes.

DOI: 10.1103/PhysRevFluids.9.053907

I. INTRODUCTION

Fuel-flexible hydrogen-fired gas turbines are gaining broad interest amid a global transition to carbon-free energy production [1–4]. The addition of hydrogen to natural gas in the fuel stream of a gas turbine can significantly reduce its CO_2 emissions as well as enhancing its overall power output and efficiency [5]. However, the increased reactivity and diffusivity of hydrogen can increase the flame speed and the resistance to aerodynamic strain, impairing the static and dynamic stability of

*by.uk.ahn@gmail.com

the overall system. Static stability issues can include flame flashback, where the flame propagates upstream from its intended anchoring location, potentially causing costly engine damage. Dynamic stability issues can include combustion instabilities, also known as thermoacoustic instabilities, in which the coupling between heat-release-rate (HRR) and pressure oscillations can lead to a self-excited feedback loop that yields damaging flow oscillations in the combustor. The ability of hydrogen flames to withstand higher strain rates enables them to be operated over a different range of velocities and equivalence ratios in comparison with conventional hydrocarbon flames, resulting in marked changes to the flow and flame time scales. Thus the addition of hydrogen has been observed to change the relative timing between the pressure and HRR oscillations of a combustor, which can either weaken thermoacoustic instabilities [6–9] or strengthen them [10–12]. Thermoacoustic instabilities present a major challenge for the development of fuel-flexible gas turbines. Thus characterizing and understanding the complexities of such instabilities, especially their response to transient operating conditions [13], is crucial to designing more efficient and reliable gas turbines.

Gas turbines deployed for power production typically have a combustor geometry that is annular, with several flames distributed around the annulus. This geometry can give rise to azimuthal thermoacoustic instabilities, which have been observed both experimentally and numerically in a variety of industrial systems [14–17] and laboratory-scale systems [18–21]. Such azimuthal modes are characterized not only by their amplitude and frequency but also by their nature (i.e., spinning, standing, or mixed) and orientation, as defined by the antinodal line of the standing component. Even when the operating conditions are kept nominally steady, the mode nature, orientation, and amplitude can still vary markedly in time. Such behavior is known collectively as the *modal dynamics* and can be linked to turbulence-induced noise [15] and system asymmetries [22].

Annular combustors can host not only azimuthal modes, but also longitudinal modes, which are characterized by the propagation of acoustic waves in the bulk-flow direction. Recently, intermittency and secondary bifurcations have been investigated for such longitudinal modes in a premixed swirl-stabilized annular combustor [23,24]. The preferential generation of azimuthal or longitudinal modes in an annular combustor can depend on the operating conditions, such as the equivalence ratio or the mass flow rate of the reactant stream [19,25], as well as the fuel type used [18]. However, it is important to note that azimuthal and longitudinal modes can be simultaneously generated. Previous studies [25,26] have identified an operating regime where phase-coupled azimuthal and longitudinal modes coexist. This regime was associated with a *slanted* mode based on the HRR pattern [26]. The coexistence of azimuthal and longitudinal modes at the same operating condition has been experimentally verified by Fang *et al.* [27]. In that work, the two modes did not exist simultaneously, but in turn: the system intermittently alternated between them, an effect later attributed to stochastic fluctuations caused by turbulence in the high-speed reactant flow. A single mode-switch event between longitudinal and azimuthal states was observed by Mazur *et al.* [28] in an annular combustor at an elevated pressure. In that system, the mode-switch event was associated with upstream flame propagation (flame flashback), which altered the flame structure. In that [28] and other studies at elevated pressure [9,13,29], high amplitude instabilities with significant harmonic content were observed, further complicating the interpretation of the modal dynamics of the system.

Although mode switching can occur even when the operating conditions are held nominally steady in time, it is of interest to understand how thermoacoustic modes can change in response to varying the operating conditions in time. One practical motivation for this is to identify early warning signals of thermoacoustic instability as a combustion system is adjusted from one power setting to another. Many previous studies in thermoacoustics have examined the use of transient operating conditions, but they were mostly limited to single-flame configurations [30–32]. Recent studies have focused more on the use of transient operating conditions in annular combustors [25,29], but to date only one study, focusing on azimuthal modes, has been performed under elevated pressure [13]. Improving our understanding of the onset, growth, and interaction of different thermoacoustic modes during transient operation at elevated pressures could help researchers limit the occurrence

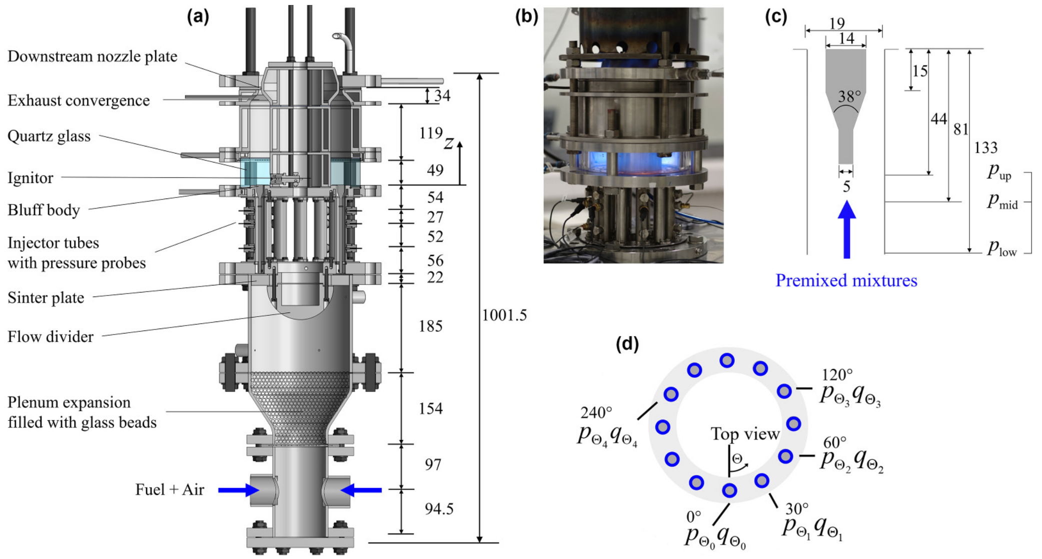

FIG. 1. IPA rig and combustor instrumentation: (a) cross-sectional view with dimensions in mm, (b) photograph of the combustor during operation, (c) close-up diagram showing the injector dimensions, and (d) overhead view showing the azimuthal arrangement of the pressure sensors and photomultiplier tubes.

and severity of self-excited thermoacoustic instabilities in practical combustion systems such as gas turbines. Over the years, various system identification tools have been developed and tested to better understand and characterize the behavior of thermoacoustic instabilities [33–36]. These typically involve applying a variety of time-series methods to the pressure or HRR signals in order to identify subtle changes at the onset of a bifurcation to a thermoacoustically unstable state. Again, while these methods have previously been applied to single-flame combustion systems, they have yet to be applied to annular systems in which both longitudinal and azimuthal modes may exist simultaneously.

This experimental study investigates the self-excited thermoacoustic modes of a pressurized annular combustion system powered by methane-hydrogen flames under both steady and transient operating conditions. During transient operation, high-amplitude longitudinal and azimuthal modes are simultaneously generated. Automated mode-detection tools are applied to the pressure and HRR time-series data in order to identify the various instability regimes. Time-series analysis tools are also used to characterize the intermittency features, including identifying the specific intermittency type. The results are then explained in terms of changes in the modal dynamics and harmonic content of the system.

II. EXPERIMENTAL SETUP

A. Intermediate pressure annular (IPA) combustor

In this investigation, we used the Intermediate Pressure Annular (IPA) combustor, whose key features are described briefly below and in Fig. 1. For full details, please refer to [13,28,29]. Premixed reactants at 293 K entered a plenum chamber before passing through a bed of glass beads and an acoustically reflective 22 mm thick sintered metal plate. This plate has a porosity of 0.12, a mean pore size of 183 μm, and a pressure drop of $\Delta p \approx 15$ kPa at the flow rates used in the present study [29]. The reactant mixture was distributed to the combustor via 12 injector tubes, each with an inner diameter of $D_{\mathrm{inj}} = 19$ mm and a centrally mounted bluff body of diameter $D_{\mathrm{bb}} = 14$ mm, as shown in Fig. 1. The flow swirlers used in previous studies [29] were removed for this study.

TABLE I. Operating conditions.

P_H	V_H	ϕ	S_L (ms^{-1})	$\dot{m}_{air}$ (gs^{-1})	$\dot{m}_{fuel}$ (gs^{-1})	Thermal power (kW)	Cooling power (kW)
0.3	0.57	0.5–1.1	0.43–0.45	63.8, 74.4, 85.0	1.9–5.5	92.8–272.3	16.7–110.2
0.4	0.67	0.5–1.1	0.47–0.49	63.8, 74.4, 85.0	2.5–7.3	95.3–279.6	16.1–119.0
0.5	0.75	0.5–1.1	0.50–0.53	63.8, 74.4, 85.0	3.1–9.1	97.9–287.2	16.4–111.4

The combustor had a length of 168 mm with inner and outer diameters of $D_i = 128$ mm and $D_o = 212$ mm, respectively. The lower section (49 mm) of the outer wall was constructed from quartz for optical access. The combustor was equipped with multiple water paths for cooling and the inlet and exit temperatures were monitored. An area reduction occurs at the exit of the combustor, defined by a fifth-order polynomial of length $L_{CR} = 34$ mm and a contraction ratio of $CR_c = 7$. Downstream of this contraction was a choking plate of $CR_p = 5$, resulting in a total contraction ratio of $CR_{tot} = 35$.

The test conditions are summarized in Table I. The laminar flame speed, S_L, was estimated using Cantera [37] with the GRI 3.0 mechanism for the combustion kinetics. Methane-hydrogen blends were used, with the air and fuels (CH_4 and H_2) metered by four Alicat mass flow controllers (MFCs). The volume fraction of hydrogen, $V_H = \dot{V}_{H_2}/(\dot{V}_{CH_4} + \dot{V}_{H_2})$, varied between 0.57 and 0.73. This equates to a thermal power ratio of hydrogen from $P_H = P_{H_2}/(P_{CH_4} + P_{H_2}) = 0.3$ to 0.5. A range of air mass flow rates (from 63.8 to 85.0 gs^{-1}) and equivalence ratios ($\phi = 0.6$ to 1.1 in steps of 0.1) were used, producing bulk inlet flow velocities ranging from 22.9 to 29.7 ms^{-1} and mean pressures of 141 to 232 kPa. The uncertainty was estimated as ± 0.01 for the equivalence ratio and ± 0.04 ms^{-1} for the bulk velocity. These estimates represent the average uncertainty values for a single injector, although larger injector-to-injector differences may be present [38], Fig. 5].

The present paper focuses on a final operating point at $P_H = 0.4$, $\dot{m}_{air} = 74.4$ gs^{-1}, and $\phi = 1.1$. This point was reached by linearly increasing the equivalence ratio from $\phi = 0.5$ to 1.1, over three different ramping times: $t_R = 2$, 5, and 10 s. At $\phi = 0.5$ and 1.1, the thermal power is 111.2 and 244.7 kW, respectively. The heat transfer from the flame zone to the combustor walls included contributions from the bottom plate forming the dump plane ($P_{cool\text{-}d}$), the inner wall ($P_{cool\text{-}i}$), and the outer wall ($P_{cool\text{-}o}$). At $P_H = 0.4$ and $\dot{m}_{air} = 74.4$ gs^{-1}, the cooling power in these paths was measured as $P_{cool\text{-}d} = 0.7$, $P_{cool\text{-}i} = 3.9$, and $P_{cool\text{-}o} = 7.8$ kW for the $\phi = 0.5$ case and $P_{cool\text{-}d} = 8.1$, $P_{cool\text{-}i} = 62.8$, and $P_{cool\text{-}o} = 30.7$ kW for the $\phi = 1.1$ case.

The time delay between setting the MFC output and the mixture reaching the combustor chamber was estimated as 0.3 ± 0.01 s, based on the pipe lengths, diameters, and the volume flow rates of the premixed reactants. After this time delay was accounted for, the start of the ϕ ramping, $t = 0$ s, aligned with the actual change in equivalence ratio in the combustor. The combustor was cooled down after each test and a minimum of three repeat measurements were taken at each operating condition.

B. Instrumentation and data acquisition

Twelve Kulite XCE-093 pressure transducers, with a sensitivity of 1.4286×10^{-4} mV/Pa, were installed in the injector ducts to characterize the thermoacoustic modes. Nine transducers were mounted at three circumferential locations ($\Theta_{k=1,3,4} = 30$, 120, and 240°) and at three axial locations, all upstream of the dump plane ($z = -44, -81,$ and -133 mm). Two transducers were mounted at $z = -81, -133$ mm and $\Theta_{k=0} = 0°$ and one transducer was mounted at $z = -81$ mm and $\Theta_{k=2} = 60°$. The signals from the pressure transducers were conditioned via a Fylde FE-579-TA amplifier, before undergoing digitization by a 16-bit NI 9174 DAQ system at a sampling rate of 51.2 kHz.

Photomultiplier tubes (PMT) equipped with UV filters [305(10) nm] were also installed at five circumferential locations ($\Theta_{k=0,1,2,3,4} = 0$, 30, 60, 120, 240°). They were mounted at a distance of

244(3) mm from the center of the bluff body, aligned in the radial direction, at a height of 20 mm above the dump plane.

Two high-speed cameras (Phantom V2012) equipped with intensifiers and the same UV filters [305(10) nm] were positioned at $\Theta = 30^\circ$ and 120°. The flame images were not analyzed in the present study, but readers interested in viewing the corresponding flame shapes and HRR distributions are referred to [39].

The temperature was measured with a K-type thermocouple mounted in the outer annular wall at $\Theta = 0^\circ$, 187 mm downstream of the dump plane. The tip of the thermocouple protruded 5 mm into the combustion chamber.

III. MATHEMATICAL FRAMEWORK FOR DATA ANALYSIS

A. Azimuthal mode characterization

The amplitudes of the thermoacoustic modes were extracted at $z = -81$ mm as this particular axial location hosted a large number of sensors. In this paper, overline notation $(\bar{\cdot})$ is used to denote time averaging, while dash $(\cdot')$ and hat $(\hat{\cdot})$ notations are used to denote fluctuations in the time and frequency domains, respectively. Azimuthal modes can be examined via upstream measurements made in the injector ducts owing to the injector-combustor coupling, which is similar to that described by [40]. This implies that pressure oscillations in the annulus result in flow oscillations in the injector ducts. The details of this method are described in [38].

To characterize the fundamental mode ($n = 1$), the pressure time series was bandpass filtered with a bandwidth of 50 Hz centered around the frequency of interest. Following Ghirardo and Bothien [41], the acoustic pressure oscillations in the annulus of the combustor were resolved as

$$p'(\Theta, t) = A\,\cos[n(\Theta - \theta)]\cos(\chi)\cos(\omega t + \varphi) + A\,\sin[n(\Theta - \theta)]\sin(\chi)\sin(\omega t + \varphi), \tag{1}$$

where Θ is the azimuthal coordinate and n is the order of the mode. Four state space variables are used to describe the mode: A is the amplitude of the mode, $n\theta$ is the position of the antinodal line (which is bounded between 0 and 180°), χ denotes the nature of the azimuthal mode and is often known as the *nature angle*, and φ is the temporal phase. Here a mode is standing if $\chi = 0^\circ$, is spinning clockwise or counterclockwise if $\chi = \mp 45^\circ$, or is a mix of both if $0^\circ < |\chi| < 45^\circ$. The sign convention for the spin direction is based on a top-down view of the combustor, consistent with the coordinate system shown in Fig. 1.

B. Synchronization analysis

The Kuramoto order parameter, R, can be used to quantify the degree of synchronization between thermoacoustic oscillations in different burners, as described in [42]

$$R(t) = \frac{1}{N_\mathrm{b}}\left|\sum_{k=1}^{N_\mathrm{b}} \exp[i\psi_k(t)]\right|, \tag{2}$$

where ψ_k is the phase of the oscillations in the kth burner, calculated via the Hilbert transform, while N_b is the total number of burners in the synchronization analysis. The parameter R has values between 0 and 1: 0 indicates the absence of synchronization, while 1 indicates the complete synchronization of oscillations in different burners.

In this study, focus is directed at the burners equidistantly spaced at $\Theta = 0$, 120, and 240°. This configuration yields a Kuramoto order parameter of $R = 1$ for a perfectly longitudinal mode and $R = 1/3$ for any perfectly azimuthal mode of the first order.

C. Automated mode detection

In this study, the approach of Lee [43] was used for automated mode detection. This involved combining the permutation entropy, the Jensen-Shannon complexity, and an unsupervised clustering algorithm. These techniques are outlined briefly below; a more detailed description can be found in [43].

The permutation entropy, PE, is a quantitative measure of the complexity of a time series and can take on values between 0 and 1: 0 indicates purely stochastic dynamics, while 1 indicates deterministic behavior [44]. The computation of PE involves first segmenting a time series into small sections of length D_{PE}, where D_{PE} is an integer representing the number of samples. Within each section, the data values are compared against their neighbors to determine whether they are increasing or decreasing. Given the predetermined length of each section, there can only be a set number of possible permutations, represented as $D_{PE}!$. The combined probability of the permutations observed in all the data sections is computed and then normalized by the total number of possible combinations to yield the permutation entropy. In this study, the sample length was chosen as $D_{PE} = 5$ in line with [43], and the time delay between adjacent data points was set as $\tau_{PE} = 1$, implying that adjacent data points were separated in time by the reciprocal of the acquisition frequency.

The Jensen-Shannon complexity [45], C, can be used to quantify the difference between the probability density function (PDF) of a time series and a continuous uniform distribution; it can take on values between 0 and 1. It works differently from PE, but can still reveal valuable insight into the dynamical structures embedded in a time series. When combined together, PE and C are particularly effective in revealing subtle variations in time series data [43].

As per Lee [43], these metrics were applied to time traces of the pressure and global HRR fluctuations. In this way, three-dimensional scatter plots were generated, facilitating the classification of various temporal features. To achieve such classification, k-medoids unsupervised clustering was applied [46], which involved grouping similar data points together and separating dissimilar data points. The effectiveness of this automated algorithm in detecting different dynamical states will be assessed in Sec. IV B.

D. Phase space reconstruction

Phase space reconstruction is an established technique used to visualize and analyze the evolution of a nonlinear dynamical system. In this study, phase space reconstruction was performed using Takens' time-delay embedding theorem [47], with the normalized pressure fluctuation $p'/\overline{p}$ of length N as the sole scalar input. The time series was embedded into a Euclidean vector of dimension d:

$$P'(d) = \{p'_i/\overline{p}, p'_{i-\tau}/\overline{p}, p'_{i-2\tau}/\overline{p}, \dots, p'_{(i-(d-1)\tau)}/\overline{p}\}, \tag{3}$$

where τ is the time delay and the index $i = (d-1)\tau + 1, \dots, N$ denotes the ith reconstruction of the state vector [48]. The optimal time delay ($\tau = 10$) was determined from the first local minimum of the average mutual information function [49]. The optimal embedding dimension ($d = 3$) was chosen based on the false nearest neighbors algorithm [50].

E. 0–1 test

In principle, the Lyapunov exponent can be used to identify chaotic processes [51,52]. However, the results become difficult to interpret when the experimental data is from a turbulent system exposed to various noise sources, either intrinsic or extrinsic, resulting in a positive Lyapunov exponent even for regular (nonchaotic) attractors, such as limit cycles or torus structures [53,54]. By contrast, the 0–1 test can be a more reliable tool for detecting chaos, even in experiments where significant noise is present [54,55]. In this binary test, the translation variables, $\mathcal{M}_c(n_i)$ and $\mathcal{N}_c(n_i)$, are calculated from a normalized pressure time series $p'_j/\overline{p}$ (where $j = 1, \dots, N$) [55]:

$$\mathcal{M}_c(n_i) = \sum_{j=1}^{n_i} (p'_j/\overline{p}) \cos(jc), \tag{4}$$

$$\mathcal{N}_c(n_i) = \sum_{j=1}^{n_i} (p'_j/\overline{p}) \sin(jc), \tag{5}$$

where $n_i = 1, 2, \dots, N$ and c is a constant value. In this study, c was randomly selected as $c \in [3\pi/10, 3\pi/5]$, falling within the suggested range $(\pi/5, 4\pi/5)$ [54,56]. The computation of the translation variables is dependent on the value of n_i, where $n_i \leqslant n_{\text{cut}}$. In practice, with a finite length time series, n_{cut} should be much smaller than the total number of variables N and is typically chosen to be $n_{\text{cut}} = N/10$ [55,57]. The diffusive behavior of the trajectory in the $[\mathcal{M}_c, \mathcal{N}_c]$ plane for increasing n_i was further investigated via the mean squared displacement $D(n_i)$:

$$D(n_i) = \lim_{N\to\infty} \frac{1}{N} \sum_{j=1}^{N} \{[\mathcal{M}_c(j + n_i) - \mathcal{M}_c(j)]^2 + [\mathcal{N}_c(j + n_i) - \mathcal{N}_c(j)]^2\}. \tag{6}$$

For improved convergence of $D(n_i)$, a modified mean squared displacement $M(n_i)$ with the same growth rate was used [56,58]:

$$M(n_i) = D(n_i) - V_{\text{osc}}(c, n_i), \tag{7}$$

where

$$V_{\text{osc}}(c, n_i) = \left[\lim_{N\to\infty} \frac{1}{N} \sum_{j=1}^{N} (p'_j/\overline{p})\right]^2 \frac{1 - \cos(nc)}{1 - \cos(c)}. \tag{8}$$

Here $M(n_i)$ increases progressively for chaotic attractors but oscillates within bounds for regular (nonchaotic) attractors. Moreover, the asymptotic growth rate of the mean squared displacement was found via linear regression [56]:

$$K = \text{corr}(\xi, \Delta) = \frac{\text{cov}(\xi, \Delta)}{\sqrt{\text{var}(\xi)\text{var}(\Delta)}} \in [-1, 1], \tag{9}$$

where

$$\xi = (1, 2, \dots, n_{\text{cut}})^T, \tag{10}$$

$$\Delta = [M(1), M(2), \dots, M(n_{\text{cut}})]^T. \tag{11}$$

To mitigate the effect of outliers, the calculation of K was repeated a total of $N_c = 200$ times, as suggested by Gottwald *et al.* [56]. Then, the median of N_c values of K, denoted as K_m, was estimated. In the 0–1 test, the value of K_m approaches 0 for regular dynamics, but approaches 1 for chaotic dynamics [56,59].

F. Autocorrelation function

The autocorrelation function (ACF) is another tool for identifying chaos and has been successfully used on various experimental systems, such as a periodically forced neon glow discharge and a self-excited flame-driven combustor [60,61]. For a given time series, it enables regular and chaotic dynamics to be differentiated by quantifying the similarity between the original time series and time-lagged copies of that series. The ACF is typically presented as a plot of the autocorrelation coefficient R_k versus the lag k of the input normalized time series $p'(t)/\overline{p}$ [62]. The N successive observational values of $p'(t)/\overline{p}$ made at equispaced instants $t, t + \Delta t, t + 2\Delta t, \dots, t + (N - 1)\Delta t$

are denoted as $\{p'_1/\overline{p}, p'_2/\overline{p}, p'_3/\overline{p}, \ldots, p'_N/\overline{p}\}$, where Δt is a fixed time lag. Therefore, the delayed copy, $p'(t+k)/\overline{p}$, of $p'(t)/\overline{p}$ separated by k time intervals has a length of $N-k$ and the observational values are $\{p'_{t+k}/\overline{p}\}_{t=1}^{N-k}$. The R_k between $p'(t)/\overline{p}$ and $p'(t+k)/\overline{p}$ at lag k is defined [62]:

$$R_k = \frac{c_k}{c_0}, \tag{12}$$

$$c_k = E[(p'_t/\overline{p} - \mu), (p'_{t+k}/\overline{p} - \mu)] = \frac{1}{N}\sum_{t=1}^{N-k}(p'_t/\overline{p} - \mu)(p'_{t+k}/\overline{p} - \mu), \tag{13}$$

where $\mu = \frac{1}{N}\sum_{t=1}^{N}(p'_t/\overline{p})$ is the mean of $p'(t)/\overline{p}$. The ACF would then be calculated from R_k for $k = 0, 1, 2, \ldots, K$, where $K \leqslant N/4$ [62]. For a regular time series, the ACF exhibits strong similarities in time, resulting in long-range correlations. By contrast, the correlation is much shorter in time for chaotic signals. Thus, as the time lag increases, the ACF for a chaotic signal decays rapidly towards 0, but that for a regular signal decays gradually towards 0.

G. Recurrence plot

The recurrence plot (RP), first proposed by Eckmann *et al.* [63], has been used in various fields of science and engineering to characterize the recurrence properties of nonlinear dynamical systems [64,65]. The construction of the RP involves computing a binary matrix $R_{i,j}$ based on a reconstructed phase space. This matrix captures the distance between pairs of data points on the phase space trajectory. For a phase trajectory P' with points N, the recurrent matrix $R_{i,j}$ is denoted as

$$R_{i,j} = \mathcal{H}(\epsilon - ||P'_i - P'_j||), \quad i, j = 1, \ldots, N, \tag{14}$$

where $P'_i \in \mathbb{R}^d$ represents a state observed at time i and N is the number of considered states in the d-dimensional phase space. $\mathcal{H}$ is the Heaviside step function and ϵ is a recurrence threshold used for determining the recurrent property of a pair of phase trajectory points. Recurring pairs of phase points that satisfy the criterion $\epsilon \leqslant ||P'_i - P'_i||$ generate filled-in (dark) patterns in the RP, while nonrecurring pairs of phase points ($\epsilon > ||P'_i - P'_i||$) generate empty (light) patterns. Previous studies have shown that RPs exhibit different characteristic patterns for different types of intermittency [65–67]. For instance, for Pomeau-Manneville intermittency [68], kitelike structures appear for type-II intermittency (Fig. 14 in Ref. [65]) but rounded upper-right corners appear for type-III intermittency (Fig. 15 in Ref. [65]). Thus the RP can be used to identify the type of intermittency exhibited by a dissipative dynamical system. In the present study, the recurrence threshold ϵ was set at 18% of the largest attractor dimension with an embedding dimension of $d = 9$ and a time delay of $\tau = 10$.

IV. RESULTS AND DISCUSSION

The present paper focuses on the operating point at $P_{\mathrm{H}} = 0.4$, $\dot{m}_{\mathrm{air}} = 74.4\,\mathrm{gs}^{-1}$, and $\phi = 1.1$, where high-amplitude azimuthal modes are present. At this operating point, the mean pressure is $\bar{p} = 197.6\,\mathrm{kPa}$ and the mean bulk flow velocity is $\bar{u} = 23.7\,\mathrm{ms}^{-1}$. This point is examined under both steady and transient operating conditions, representing the target of an equivalence-ratio ramp. For reference, the stability of the different operating points listed in Table I is described in the Appendix.

A. Mode transition during equivalence-ratio ramping

Figure 2 shows the transient behavior of the system leading to the onset of an azimuthal instability at $\dot{m}_{\mathrm{air}} = 74.4\,\mathrm{gs}^{-1}$, $\phi = 1.1$, and $P_{\mathrm{H}} = 0.4$. At $t = 0\,\mathrm{s}$, the equivalence ratio was increased linearly from $\phi = 0.5$ to 1.1, with the different columns in Fig. 2 corresponding to different ramping times, from left to right: $t_{\mathrm{R}} = 2$, 5, and 10 s.

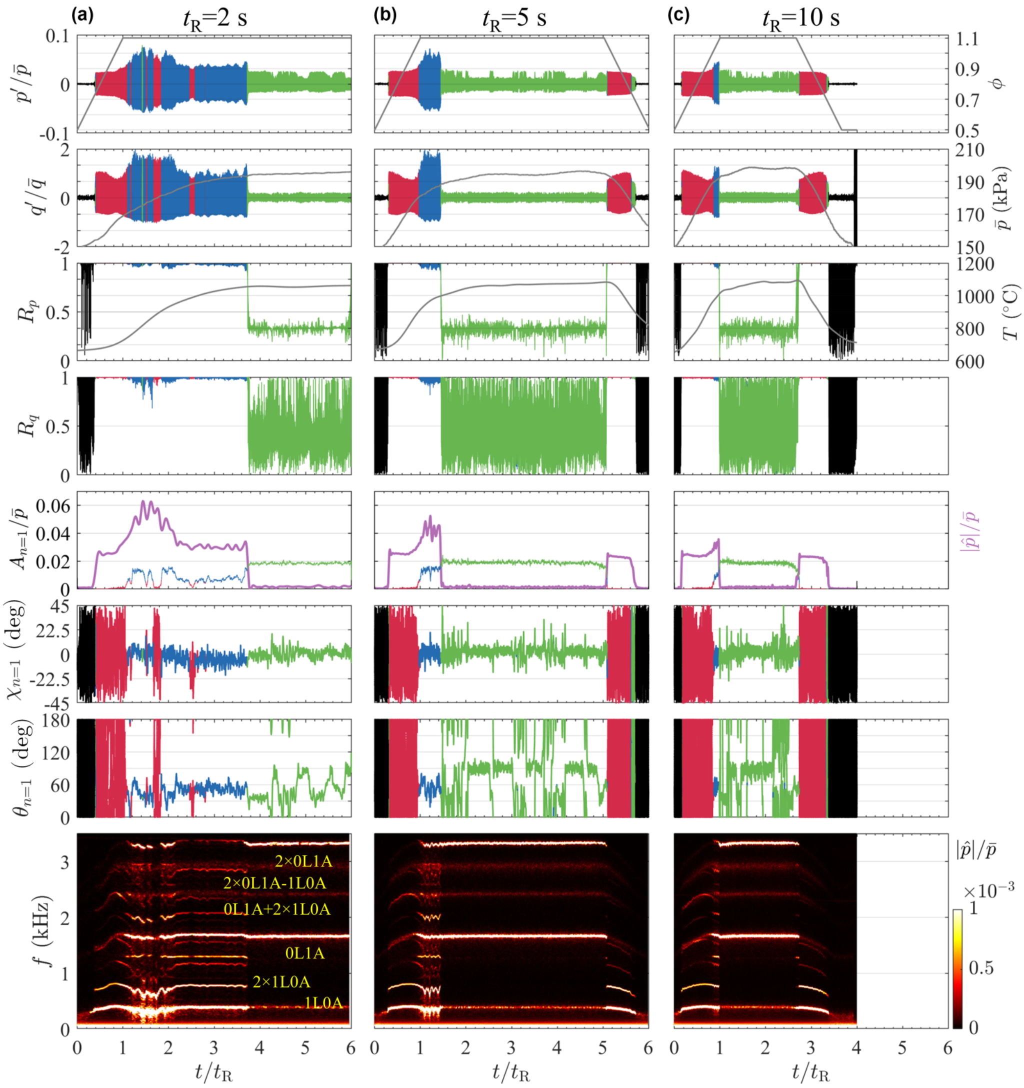

FIG. 2. Time series analysis during ramping of the equivalence ratio at three different time scales, from left to right: $t_R = 2$, 5, and 10 s. Starting from the top, rows 1 and 2 show time traces of the pressure (at $\Theta = 30°$, $z = -81$ mm) and HRR (at $\Theta = 30°$) oscillations, respectively. Rows 3 and 4 show the Kuramoto order parameter for pressure and HRR using signals measured at three orientations: $\Theta = 0$, 120, and 240°. Rows 5, 6, and 7 show the normalized azimuthal and longitudinal mode amplitude ($A/\bar{p}$ and $|p'|/\bar{p}$), the nature angle (χ), and the orientation angle (θ). At the bottom, row 8 shows the spectrogram of the normalized pressure signal, computed using short time (0.1 s) FFTs with Hanning windowing. In rows 1, 2, and 3, the gray lines show the time-varying equivalence ratio, mean chamber pressure, and downstream chamber temperature, respectively. In rows 1 to 7, the dynamical states are categorized as 0L0A (combustion noise; black), 1L0A (longitudinal mode; red), 0L1A (azimuthal mode; green), and 1L1A (transitional state; blue). These color-coded regimes are based on the clustering results from Sec. IV B.

The gray lines in the top three rows represent the normalized temporal variation (t/t_R) of the equivalence ratio, the mean pressure, and the mean temperature. As the equivalence ratio increases, both the mean temperature and pressure increases. A slight delay between ϕ, $\bar{p}$, and T appears in the

$t_R = 2$ s case. This delay decreases as the ramping time increases, with better correlation between ϕ, $\bar{p}$, and T.

The spectrograms at the bottom of Fig. 2 reveal the complex dynamical response of the system. Starting with the $t_R = 2$ s case on the left, the combustor is initially thermoacoustically stable ($t/t_R = 0$), with only faint spectral lines at 325 Hz and 1.4 kHz, which correspond to incipient longitudinal and azimuthal modes. As ϕ increases at $t/t_R \approx 0.5$, the system exhibits a strong longitudinal mode, whose fundamental frequency increases rapidly with the combustor temperature as ϕ increases, peaking at around 375 Hz. Weaker higher-order harmonics are also observed. At $t/t_R = 1$ when $\phi = 1.1$, a high-amplitude azimuthal mode is also generated alongside the existing longitudinal mode, with both the fundamental and harmonics clearly visible. Over the next ~4–5 s, these two modes coexist and begin to interact, as evidenced by the significant spectral content at the difference between the fundamental azimuthal and longitudinal mode frequencies ($f \approx 1300$ Hz). At $t/t_R = 3.7$, the longitudinal mode decays, leaving only the azimuthal mode. After the decay of the longitudinal mode, the frequency of the azimuthal mode is observed to decrease slightly. The azimuthal mode remains pronounced until a ramp down to $\phi = 0.5$, when the system returns to a thermoacoustically stable condition via the longitudinal mode. For brevity, the latter case is not shown for the $t_R = 2$ s condition, but is observable in cases with a longer ramping time.

In Fig. 2, the mode amplitude is highlighted by the spectrogram color, but this can be seen more readily in the top two rows, which show time traces of the normalized pressure ($p'/\bar{p}$) and HRR ($q'/\bar{q}$) fluctuations at a single azimuthal measurement location ($\Theta = 30^\circ$); for the pressure signal, the axial location is $z = -81$ mm.

The time series data for these and subsequent plots are colored in blue, red, and green, which relate to the automated mode detection discussed later in Sec. IV B. The envelopes of the signals show the onset of the longitudinal mode at $t/t_R = 0.5$, with a marked increase in the amplitude occurring at $t/t_R = 1$ owing to the onset of the azimuthal mode. Large amplitude fluctuations are observed until $t/t_R \approx 2$. A sudden decrease in amplitude occurs at $t/t_R \approx 3.7$ with the decay of the longitudinal mode. After $t/t_R \approx 3.7$, the pressure signal during the generation of azimuthal modes is observed to be intermittent, which is discussed in detail in Sec. IV D.

The amplitude of each modal component can be more readily analyzed by isolating and plotting the time series of $|\hat{p}|/\bar{p}$ for the longitudinal mode and that of $A/\bar{p}$ for the azimuthal mode, as shown in the fifth row of Fig. 2. When the longitudinal mode emerges, $|\hat{p}|/\bar{p} \approx 0.02$, but following the onset of the azimuthal mode, the longitudinal mode exhibits significantly larger amplitudes (up to $|\hat{p}|/\bar{p} \approx 0.06$). In the case of $t_R = 2$ s, the azimuthal mode is observed to be intermittent during the initial transient phase, demonstrating moderate amplitudes until the final limit cycle is reached after the decay of the longitudinal mode.

The changes in the dominant modes are also apparent in the Kuramoto order parameter for pressure (R_p) and HRR (R_q), shown in the third and fourth rows of Fig. 2, respectively. The value of R_p fluctuates wildly in the absence of a coherent self-excited instability, but, at the onset of the longitudinal mode, it approaches $R_p \approx 1$. This indicates in-phase oscillations at multiple azimuthal locations, which is consistent with the presence of a global longitudinal mode. Weak fluctuations in R_p near unity are observed when both the longitudinal and azimuthal modes exist simultaneously, but R_p only decreases significantly at $t/t_R = 3.7$, with the decay of the longitudinal mode. The azimuthal mode leads to $R_p \approx 1/3$, which is consistent with the combined action of in-phase and out-of-phase motion expected during an azimuthal instability. The value of R_q exhibits broadly similar characteristics, but with a significantly higher level of variability during the azimuthal mode. This greater variability reduces the reliability of R_q, making it less effective than R_p for identifying the dominant mode.

The azimuthal mode can be examined in more detail through the time series of χ and θ, as shown in the sixth and seventh rows of Fig. 2. At low A, the mode nature and orientation angles are dominated by noise. However, with the onset of strong azimuthal modes, predominantly standing waves are generated with slight fluctuations between slightly positive and negative nature angles. The longitudinal and azimuthal modes coexist, but there is a preferred orientation angle of $\theta \approx 30$ to

60°. After the longitudinal mode decays, this preferred orientation angle changes slightly, oscillating between two relatively stable values at $\theta = 30^\circ$ and 90°.

These modal observations are confirmed by statistical analysis performed over the entire duration of the stable high-amplitude regimes for multiple test runs (not shown for brevity). Previous investigations of nonswirling flames at atmospheric pressure have revealed a tendency for the generation of spinning waves at high amplitudes [69]. Furthermore, at very high instability amplitudes, swirling flames in the same combustor geometry always provoke strongly spinning modes [29]. The modal preference observed in the present study may be caused by reduced symmetry [15,70] or by the susceptibility of flames to transverse perturbations [71]. As shown in the time series, the antinodal line is aligned preferentially at $\theta = 30^\circ$ and 90°, indicating that the configuration is slightly asymmetric. This behavior is consistent with that observed in previous experiments [18], which unavoidably contains a minor degree of asymmetry owing to production tolerances and individual component variations [38], Fig. 5].

Thus far, the analysis has focused on the case of $t_R = 2_S$, but results for the other two ramping times ($t_R = 10_S$) show broadly similar phenomena. A comparison across the different ramping times demonstrates that the onset of the initial longitudinal mode is not a function of pressure or downstream temperature and occurs at slightly different equivalence ratios for the three cases. Notable differences are also observed in the amplitude of the self-excited thermoacoustic oscillations. Increasing the ramping time (i.e., decreasing the ramping rate) leads to decreases in both the peak amplitude of the longitudinal mode as well as the duration when the longitudinal and azimuthal modes are simultaneously present. Therefore, it is preferable to ramp slowly if the aim is to limit the peak amplitudes of the thermoacoustic modes. Ramping slowly also reduces the frequency and amplitude of the longitudinal mode modulations, while eliminating intermittency during the onset of the azimuthal mode.

B. Automated mode detection

Figure 3 presents the results of the automated mode detection for the case of $t_R = 2$ s. The results for the other two ramping times are similar and are thus omitted for brevity. The permutation entropy and Jensen-Shannon complexity are presented in Figs. 3(a) and 3(b) for the pressure and HRR signals, respectively. The permutation entropy (open circular symbols) is shown to vary in time, with different characteristic values observed during mode onset and the occurrence of different mode combinations. Before the onset of high-amplitude instability, PE_p has a value of around 0.38. When the system is dominated by longitudinal, simultaneous longitudinal-azimuthal, and azimuthal modes, PE_p has characteristic values of around 0.25, 0.35, and 0.35–0.5, respectively, with significant fluctuations observed only for the azimuthal-dominated case. The Jensen-Shannon complexity (filled circular symbols) also exhibits qualitatively similar behavior, albeit with slightly lower absolute values. The similarity of the PE_p and C_p values observed during both simultaneous longitudinal-azimuthal-mode states and dominant azimuthal-mode states may indicate that these two pressure metrics are incapable of distinguishing between the instability regimes. However, PE_q and C_q in Fig. 3(b) show clear differences, which may be due to the increased noise of the HRR measurements in comparison with the pressure measurements or due to significant differences in the flame response, such as the almost complete extinction of the flame in the presence of high-amplitude longitudinal modes [39].

The application of a clustering algorithm to both two-dimensional and three-dimensional time-series data is shown in Figs. 3(c) and 3(d), respectively. As previously discussed, the combination of pressure metrics in the two-dimensional data set results in similar values of PE_p and C_p for both simultaneous longitudinal-azimuthal modes and dominant azimuthal modes, resulting in a continuous distribution spanning low to high values. A separate cluster of data points observed just prior to $t/t_R = 0$ and exhibiting exceptionally high values is attributed to stochastic fluctuations arising from turbulent noise in the absence of thermoacoustic instability. The data are clustered based on four medoids, which physically correspond to stochastic noise, dominant longitudinal

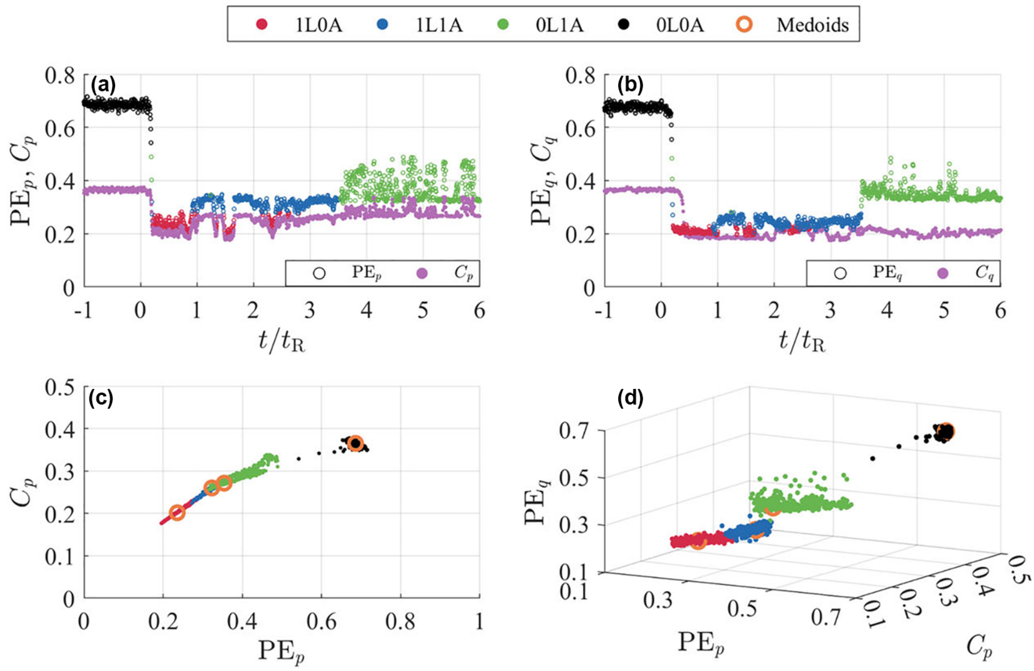

FIG. 3. Permutation entropy and Jensen-Shannon complexity for the (a) pressure and (b) heat release rate signals when $t_\mathrm{R} = 2$ s. (c) Two-dimensional complexity-entropy causality plane (CECP), a plane illustrating the interaction between the complexity and entropy of signals. (d) Three-dimensional complexity-entropy causality space (CECS), a feature space in which to better understand the categorization of signal behavior across the various regimes. Cluster centroids are identified using k-medoids clustering, as denoted by orange markers. Computations were executed with a window size of 0.1 s and a 50% overlap. The clustering patterns for the other azimuthal sensor orientations are similar, so they are omitted here to reduce redundancy.

modes, simultaneous longitudinal-azimuthal modes, and dominant azimuthal modes. The two pressure metrics, PE_p and C_p, produce well-defined upper and lower medoids, but the two intermediate medoid centers have similar values, which may lead to poor separation of some mode states.

The addition of the HRR metric PE_q in the three-dimensional data set improves the identification of the dominant azimuthal modes, resulting in a clearer distinction of this state. However, the pure longitudinal and multiple mode states still share some continuous values, which may hamper state identification. Again, the automated clustering leads to four medoids with the same physical representation as the two-dimensional data set. However, these now exhibit better separation in terms of their three-dimensional positions. The four medoids from the three-dimensional data are used to cluster the mode states, which are color coded in Figs. 2 and 3.

A clearer assessment of this classification scheme can be found in the time series of $A/|\bar{p}|$ shown previously in Fig. 2. Returning to this figure, during initial ramping of the equivalence ratio, the system is dominated by background noise, without any evidence of high-amplitude thermoacoustic instabilities (see black lines). Later, as the longitudinal mode strengthens, the $A/|\bar{p}|$ line is colored red, representing a dominant longitudinal mode. For $A/|\bar{p}| \gtrapprox 0.005$, the $A/|\bar{p}|$ line is colored blue, denoting the presence of both longitudinal and azimuthal modes. This specific threshold value was selected automatically, without user input, by the clustering algorithm, which is capable of identifying even subtle quantitative differences in the time-series features between these mode states. Finally, the decay of the longitudinal mode and the emergence of the steady high-amplitude azimuthal mode are shown in green. It is worth noting that similar mode identification could have been made by analyzing the relative amplitudes of the different spectral components, alongside

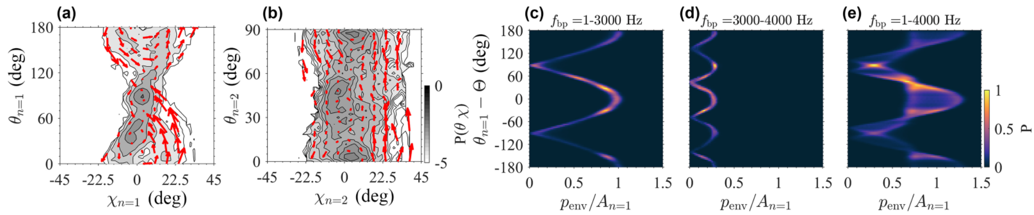

FIG. 4. JPDFs showing the correlation between mode orientation, nature angle, and amplitude during steady operation. (a) JPDF of the nature angle and mode orientation for the fundamental component and (b) the first harmonic $n = 2$, as per the approach of [72]. Probability contours are shown through base 10 exponentials. Red vector arrows indicate the mean rate of change of θ and χ. (c)–(e) Three JPDFs of the pressure envelope and orientation of the fundamental mode for different bandpass filtered frequencies, f_{bp}.

a quantification of the azimuthal mode amplitude $A/|\bar{p}|$. However, this requires *ad hoc* instability thresholds to be defined by the user, which necessitates prior knowledge of the system dynamics and limits the wider applicability of the technique to previously unseen combustors. In the automated identification routine used here, a variety of modal states can be accurately identified and differentiated even without any user input. Moreover, this classification is made on the basis of either a single pressure sensor in the two-dimensional data set or a single pressure sensor along with a single HRR monitor in the three-dimensional data set, whereas the characterization of $A/|\bar{p}|$ requires data from multiple azimuthal locations. Such time-series analysis tools are demonstrated here to provide robust utility in the unsupervised identification of azimuthal, longitudinal, and mixed modal states.

C. Modal dynamics during steady operation

As the Appendix shows, for the case of $\phi = 1.1$, $\dot{m}_{\text{air}} = 74.4\ \text{gs}^{-1}$, and $P_H = 0.4$, after the initial transient due to ramping of the equivalence ratio, the azimuthal mode dominates the system during steady operation. However, as Sec. IV A shows, even during steady operation, the modal dynamics are still azimuthal dominated, leading to significant changes in the mode orientation and nature angle, yet the mode amplitude remains relatively unchanged. To examine this, Fig. 4 presents a set of joint probability density functions (JPDFs) for different modal components during steady operation. These JPDFs are formed with data compiled from six different test runs over a total acquisition time of 52 s.

Figures 4(a) and 4(b) show the JPDFs of the orientation and nature angles for both the fundamental and first harmonic components. For the $n = 1$ mode, the system can take on every orientation, but a statistical preference emerges for orientations between $\theta = 20^\circ$ and 100°, as noted previously in the time series of Fig. 2. The most probable nature angles are near zero, confirming the predominance of standing modes. The JPDF structure consists of a high-probability streak and a low-probability donut structure centered at $\theta \approx 180^\circ$ and $\chi \approx 5^\circ$. Red vector arrows are used to highlight the mean rate of change of the orientation and nature angles, as per the approach of [72]. These form a counter clockwise trajectory around the circular JPDF pattern, producing an overall trajectory resembling a figure of 8. These characteristics indicate the most likely location of an attractor to be at $\theta \approx 90^\circ$ and $\chi \approx 0^\circ$. For the $n = 2$ mode, the modal preferences and switching patterns are broadly similar, demonstrating that these features are coupled to the fundamental mode. Greater variability, however, is seen in both the nature and orientation angles of the $n = 2$ mode, which may be ascribed to the lower signal-to-noise ratio for this specific component.

In this particular case, because the modal amplitude ($A_{n=1}$) remains relatively constant while the nature angle is near zero, the local amplitude at a specific azimuthal position is expected to be predominantly a function of the mode orientation angle. To explore this, Figs. 4(c)–4(e) show three JPDFs of the normalized pressure envelope and the normalized mode orientation angle. The JPDFs include pressure data from five different azimuthal locations, which collapse onto each other when plotted against their normalized orientation angle, $\theta - \Theta$. The pressure envelope at each orientation angle is calculated from a filtered time series using the Hilbert transform and is then normalized by the quaternion amplitude, A. Normalization of both the orientation and amplitude is performed using the fundamental component ($n = 1$). Several frequency ranges are used for bandpass filtering of the pressure signal in order to precisely isolate the subtle behavior of different modal components.

The fundamental frequency for this case is $f = 1666$ Hz. Therefore, bandpass filtering the pressure data with a frequency window of $f_{bp} = 1$ to 3000 Hz can capture the fundamental azimuthal mode ($n = 1$) and the residual spectral content from the longitudinal mode as well as other combinations of those modes, as shown in Fig. 4(c). High-probability regimes are distributed according to the modulus of a cosine function, demonstrating that the local pressure envelope for the fundamental mode is controlled by the orientation angle. This also demonstrates that the nature angle and residual longitudinal components do not appear to have a significant effect on the local pressure envelope. Bandpass filtering the data from $f_{bp} = 3000$ Hz to 4000 Hz removes the fundamental azimuthal mode, but retains the first harmonic ($n = 2$) at $f \approx 3300$ Hz, as shown in Fig. 4(d). This JPDF has a similar modulus cosine distribution, but with half the wavelength and at a lower normalized amplitude. Normalization by the fundamental amplitude leads to a first harmonic of amplitude $A_{n=2} \approx 0.3A_{n=1}$, which is consistent with the scaling reported in [29]. It should be noted, however, that as these measurements are made in the upstream injector duct, rather than in the combustor itself, any frequency dependence of the acoustic impedance (which is not characterized herein) may change this amplitude ratio in the combustor. The alignment of the pressure envelope JPDF is similar to that of the fundamental mode and, even though the orientation is normalized with respect to the fundamental component, these still collapse. This indicates a consistent spacial arrangement of the first harmonic structure with respect to the fundamental mode. Bandpass filtering the data between $f_{bp} = 1$ Hz and 4000 Hz captures the $n = 1$ and 2 azimuthal modes, producing the more unusual distribution shown in Fig. 4(e). This structure arises owing to the more complex relationship between the first- and second-order standing modes, which can contribute either constructively or destructively at a given location, depending on the mode orientation. An interesting feature is that the pressure amplitudes are no longer exceedingly low, unlike the behavior seen earlier at $\theta_{n=1} - \Theta = \pm 90^\circ$ in Fig. 4(c). These specific locations correspond to a pressure node for the $n = 1$ mode, but a pressure antinode for the $n = 2$ mode, which explains why the pressure response does not drop to near zero at those locations.

This section has demonstrated that the amplitude of the pressure response at a specific azimuthal location is mainly a function of the mode orientation. The mode orientation changes gradually over time due to the inherent modal dynamics, which depend on how the preferred mode of orientation is influenced by geometric asymmetries and noise in the system. Consequently, measurements taken at a single azimuthal location are expected to contain significant intermittency as a result of the time-varying mode orientation. Furthermore, the presence of strong harmonic components in the pressure signals is likely to profoundly affect the observed intermittency. The characteristics of intermittency and its relationship to chaos are examined in detail in the next section.

D. Intermittency and chaos

In various branches of science and engineering, it is important to identify the routes to chaos taken by a nonlinear dynamical system. This is because such routes play a key role in determining the stability and dynamics of the system during its transition from ordered to complex states, such as turbulence [73]. Characterizing such routes constitutes a vital step towards the development of tools for modeling, predicting, and controlling the system dynamics [74]. Since the 1980s, several universal routes to chaos have been established, with three of the most common being the period-doubling route, the torus-breakdown route (i.e., the Ruelle-Takens-Newhouse route), and the intermittency route [75]. For the latter route, Pomeau and Manneville [68] identified three different types of intermittency in dissipative dynamical systems: type I corresponds to a saddle-node bifurcation, type II corresponds to a Hopf bifurcation, and type III corresponds to an inverse period-doubling bifurcation. All three types of Pomeau-Manneville intermittency have been widely observed in various natural and engineered systems, demonstrating their universality [76,77].

In thermoacoustics, type-II intermittency has been observed in laminar Rijke-tube combustors operating in a thermoacoustically self-excited regime [67,78]. It has also been observed in turbulent premixed combustors where low-amplitude chaotic fluctuations (combustion noise) are gradually replaced by increasingly long, intermittent bursts of high-amplitude periodic oscillations (limit-cycle dynamics) as a bifurcation parameter is adjusted past the onset of thermoacoustic instability [79,80]. However, although there is extensive evidence of the type-II intermittency route to chaos in various laminar and turbulent combustors [23,79,80], much of the focus to date has been on longitudinal thermoacoustic modes, with relatively little attention given to the intermittency of azimuthal thermoacoustic modes.

In view of this, we performed nonlinear time-series analysis at an operating condition of $\phi = 1.1$, $\dot{m}_{\mathrm{air}} = 74.4\,\mathrm{g\,s^{-1}}$, and $P_{\mathrm{H}} = 0.4$ using data collected at an azimuthal angle of $\Theta = 0^{\circ}$ for $t_R = 2$ s [see Fig. 2(a)]. The data were analyzed after the passage of an initial transient period lasting typically $t = 8$ s, after which a statistically stationary, but intermittent, regime is reached. As noted earlier, the intermittent dynamics are attributed to the multimodal characteristics of the system (see Fig. 4). To examine how these modal components contribute to the observed intermittency, we bandpass filtered the pressure signal with a spectral window of 1–3000 Hz, thus isolating the first azimuthal mode [as per Fig. 4(c)].

Figure 5(a) shows the normalized pressure fluctuation signal $p'/\overline{p}$ at $\Theta = 0^{\circ}$. This signal (black line) consists of intermittent bursts that are strongly correlated with changes in the nature angle χ (green line) and the mode orientation angle θ (purple line). These intermittent bursts are high-amplitude periodic epochs associated with limit-cycle dynamics and tend to occur when the antinode line is oriented at $\theta \approx 30^{\circ}$. These bursts of periodicity emerge above a background of low-amplitude chaos (as confirmed below), which is observed for orientations near $\theta \approx 90^{\circ}$, consistent with the data in Fig. 4. This behavior is thought to be governed by the azimuthal mode switching. It is therefore important to identify the type of intermittency present at a specific azimuthal location, as this could reveal clues about the underlying route to chaos.

The power spectral density (PSD) of $p'/\overline{p}$ at $\Theta = 0^{\circ}$ is shown in Fig. 5(b). Consistent with the interpretation given in Sec. IV C, the pressure signal exhibits the classic signs of intermittency as proposed by Pomeau and Manneville [68]: the system switches back and forth between a regular (nonchaotic) state and a chaotic state. In the present work, intermittency is revealed by the PSD as well, which shows intermittent bursts of sharp dominant peaks during the high-amplitude epochs of periodicity. These bursts emerge above a background of broadband spectral features during the low-amplitude epochs of chaos. In phase space, the high-amplitude state corresponds to a closed repetitive orbit belonging to a limit-cycle attractor [Fig. 5(c1)], as evidenced by the appearance of two separate clusters of trajectory crossings in the double-sided Poincaré map [Fig. 5(d1)]. However, the low-amplitude state corresponds to a strange attractor [Fig. 5(c2)], as evidenced by a complex nonrepeating phase trajectory, resulting in a fractal section in the Poincaré map [Fig. 5(d2)]. This fractal behavior is confirmed by the correlation dimension, which is a topological metric used to quantify the degree of self-similarity in an attractor and was calculated here using the algorithm of Grassberger and Procaccia [81]. The results (not shown) indicate that the correlation dimension approaches a noninteger value of $\overline{D_c} \approx 5.7$ within the self-similar range of Euclidean distances. This confirms that the low-amplitude state corresponds to a strange attractor, rather than a fixed-point attractor perturbed by stochastic noise.

Two more analysis tools are used to confirm the existence of chaos in the low-amplitude state: the 0–1 test [Fig. 5(e)] and the ACF [Fig. 5(f)]. In the 0–1 test [56], the high-amplitude periodic state [Fig. 5(e1)] shows translation variables that follow a circular path with a clearly defined boundary. The mean squared displacement $M(n_i)$ is seen to oscillate within fixed bounds, leading to a growth rate of $K_m = 0$. Put together, these 0–1 test results indicate the presence of a periodic process [56,59]. By contrast, the low-amplitude chaotic state [Fig. 5(e2)] shows translation variables that follow a random walk, producing a Brownian-motion-like trajectory. The metric $M(n_i)$ is no

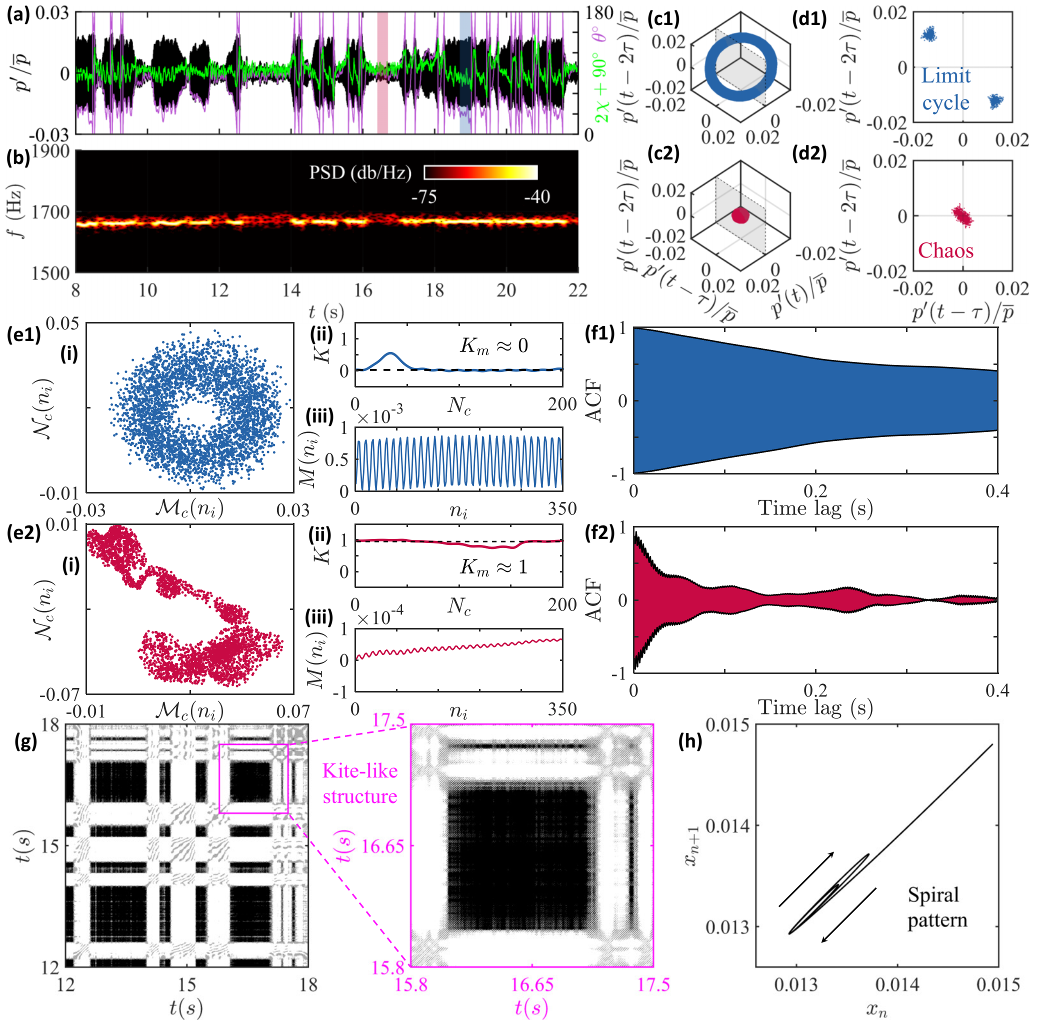

FIG. 5. (a) Time series and (b) short-time PSD of the normalized pressure fluctuation $p'/\overline{p}$ for a state of intermittency at $\Theta = 0^\circ$. Also shown are the (c) phase portraits, (d) Poincaré maps, (e) translation variables, mean displacement, and asymptotic growth rate from the 0–1 test, (f) autocorrelation function, (g) recurrence plot, and (h) first return map. In the subfigure labels, a numerical index of 1 indicates the high-amplitude limit-cycle regime (blue) and a numerical index of 2 indicates the low-amplitude chaotic regime (red). The intermittency is of the type-II Pomeau-Manneville class, as evidenced by the presence of kitelike patterns in the recurrence plot and a spiral pattern in the first return map. The pressure signal was acquired at $z = -81$ mm from the injector and was bandpass filtered with a spectral window of 1–3000 Hz.

longer bounded, but grows progressively with n_i at a rate of $K_m = 1$. These 0–1 test results are consistent with a chaotic process [54,56,59]. Next, the periodic and chaotic states are examined through the ACF. For the periodic state [Fig. 5(f1)], the envelope of the ACF decays gradually as the number of time lags increases, which is indicative of regular (nonchaotic) motion and consistent with a periodic limit cycle. By contrast, for the chaotic state [Fig. 5(f2)], the envelope of the ACF decays much more rapidly as the number of time lags increases. The ACF envelope is a wavy curve instead of a straight line, indicating the presence of short-range correlations and weak self-similarity [61,62,82].

We identify the type of intermittency present in the fundamental azimuthal mode of our annular combustor using the recurrence plot (RP) and the first return map. Figure 5(g) shows the overall RP and its magnified view for a single switching event. In both panels, the empty patches correspond to high-amplitude limit-cycle oscillations, while the filled patches correspond to low-amplitude chaos. The intermittent interruption of the chaotic epochs by strong bursts of periodicity generates a distinct checkerboard pattern. In the magnified view of the switching event, an elongated upper-right corner appears as the system transitions from chaos to limit-cycle dynamics, forming a kitelike structure. Such a structure is the hallmark sign of type-II intermittency conforming to the scenario of Pomeau and Manneville [68]. Figure 5(h) shows the first return map, where the iterates are seen forming a clear spiral trajectory. Such a spiral trajectory is another hallmark sign of type-II intermittency [83,84].

The predominance of a single azimuthal-mode frequency is characteristic of moderate amplitude instabilities, which are commonly found in atmospheric laboratory-scale annular combustors [18,38]. Here, we have experimentally demonstrated that the intermittency route to chaos can arise in the fundamental azimuthal mode of an annular combustor, broadening the universality of this transition scenario across different types of combustion systems and beyond just longitudinal thermoacoustic modes. This sets the stage for the development and application of generic control techniques formulated from chaos theory [74,85]. Moreover, we have shown that the observed intermittency conforms to type II of the Pomeau-Manneville class [68]. This specific class of intermittency is known to be amenable to modeling [75,82], suggesting that existing modeling tools from intermittency theory could be repurposed to improve the analysis and understanding of the thermoacoustic behavior of annular combustors. Finally, the discovery of the type-II intermittency route to chaos in the present system raises the possibility that the wide assortment of intermittency-based precursors [80,86,87] already developed for the early detection of thermoacoustic instability in longitudinal combustors might work on annular combustors as well.

It is worth noting that high-amplitude instabilities, induced by a choked downstream boundary at the combustor exit, can produce strong harmonic components. To explore how these components influence the intermittent dynamics, we widened the bandpass filter window to 1–4000 Hz, allowing both the fundamental azimuthal mode ($n = 1$) and its first harmonic ($n = 2$) to be included in the signal [consistent with Fig. 4(e)]. As Fig. 6 shows, notable differences can be found between the previous signal (black line: type-II intermittency route to chaos) and the new signal containing both the fundamental and first harmonic (orange line). In the latter case, intermittent switching occurs between medium- and high-amplitude periodicity (limit cycles), rather than between low-amplitude chaos and high-amplitude periodicity. The inclusion of the first harmonic has only a minor influence on the high-amplitude dynamics [Fig. 6(c1)], which remain periodic with a time-independent amplitude and a frequency at the fundamental azimuthal mode [Fig. 6(b)]. By contrast, the inclusion of the first harmonic obscures the low-amplitude chaos observed in Fig. 5, replacing it with medium-amplitude epochs containing both period-1 and period-2 dynamics at the first harmonic of the fundamental azimuthal mode [Figs. 6(c2), 6(f), and 6(g)]. This periodic behavior is clearly visible in the PSD, where the dominant spectral line alternates between $f = 1666$ and 3300 Hz [Fig. 6(b)]. In the reconstructed phase space [Figs. 6(d) and 6(e)], repetitive closed orbits are observed at different time scales, producing two and four clusters of trajectory crossings in the Poincaré map. Hence, during the medium-amplitude epochs, the system exhibits period-1 and period-2 dynamics at different time intervals. Put together, these observations concur with our assessment of the JPDF (Fig. 4): the low-amplitude chaos observed earlier can be readily obscured by the stronger fundamental and first harmonic of the azimuthal mode.

In summary, this section has revealed the profound influence that harmonic content can have on the analysis and interpretation of the intermittent dynamics of an annular combustor, even at just a single azimuthal location during changes in the mode orientation. When the fundamental azimuthal mode is isolated ($f_{bp} = 1$–3000 Hz), type-II Pomeau-Manneville intermittency between high-amplitude periodicity and low-amplitude chaos is observed. However, when the first harmonic of the fundamental azimuthal mode is included ($f_{bp} = 1$–4000 Hz), the low-amplitude chaos is

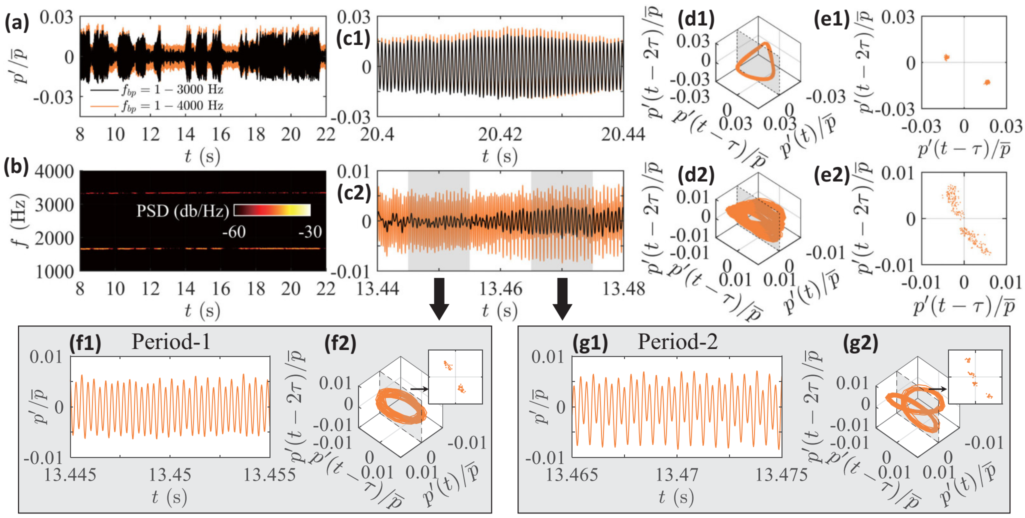

FIG. 6. (a) Time series and (b) short-time PSD of the normalized pressure fluctuation $p'/\overline{p}$ signal filtered with two different frequency bands during a state of intermittency at $\Theta = 0°$. Also shown are (c) magnified views of the $p'/\overline{p}$ signal, (d) phase portraits, and (e) Poincaré maps showing that the high-amplitude epochs correspond to a period-1 limit cycle and the medium-amplitude epochs correspond to combinational dynamics consisting of both period-1 and period-2 limit cycles. Subfigures (f) and (g) contain magnified views of the period-1 and period-2 epochs, as seen via the time series, phase portraits, and Poincaré maps. The pressure signal was acquired at a location $z = -81$ mm from the injector. The signal captures the fundamental azimuthal mode and its first harmonic, along with the longitudinal mode.

overwhelmed by intermittency between medium- and high-amplitude periodic dynamics associated with period-1 and period-2 motion.

V. CONCLUSIONS

Azimuthal thermoacoustic instabilities have been experimentally examined in a pressurized annular combustor featuring 12 bluff-body-stabilized methane-hydrogen flames. A wide range of operating conditions were investigated with the hydrogen power fraction varying from 30 to 50% ($P_{\mathrm{H}} = 0.3$ to 0.5), the air mass flow rate varying from $\dot{m}_{\mathrm{air}} = 63.8$ to 85.0 gs^{-1}, and the overall equivalence ratio varying from $\phi = 0.5$ to 1.1. These operating conditions led to a pressure ratio exceeding 1.89 across the downstream nozzle, implying a sonic exit condition.

First, the dynamic stability of the system was assessed at steady operating conditions. At a fixed hydrogen power fraction, the pressure amplitude and frequency increased with the equivalence ratio. At equivalence ratios up to stoichiometric, longitudinal modes were readily generated, but at the highest equivalence ratios, azimuthal modes were preferred. As the hydrogen power fraction was increased, the frequency of the self-excited thermoacoustic modes also increased, but their amplitudes decreased.

Next, the transient behavior leading to the onset of thermoacoustic instability was studied by carefully controlling the ramp rate of the equivalence ratio, at a single operating condition. From an initially stable state, longitudinal modes were first generated. Following this, a finite regime was identified in which both longitudinal and azimuthal modes existed simultaneously, with significant fluctuations in the modal amplitude. After some time, the longitudinal mode decays, while the azimuthal mode reaches a steady amplitude. Owing to the high amplitude of the thermoacoustic oscillations, significant harmonic content was also observed.

Automated mode detection was performed using a combination of time-series analysis tools. The permutation entropy and Jensen-Shannon complexity were used, with the former calculated with the pressure time series of a single injector and the latter calculated with both pressure and HRR data. The application of k-medoids clustering in the complexity-entropy causality space (CECS) was shown to adequately identify different modes of the system, including the stable state, both pure longitudinal and pure azimuthal modes, as well as regimes where both modes were simultaneously generated.

The high-amplitude azimuthal mode was preferentially standing in nature, with several preferred mode orientations. The modal dynamics of this configuration were investigated by studying the joint probability density functions of the different modal state space parameters and their rates of change. It was found that the modal dynamics of the first harmonic closely resembled that of the fundamental mode, implying that the pressure node of the fundamental mode is the location of a pressure antinode of the first harmonic. This finding has important implications for the intermittency behavior at the node locations, which was then analyzed in detail.

The intermittent dynamics of the fundamental azimuthal mode were investigated via phase space reconstruction, the recurrence plot, and the first return map. The intermittency manifested in the form of near-random bursts of high-amplitude periodicity on a limit-cycle attractor against a background of low-amplitude chaos on a strange attractor. The presence of chaos was verified through the 0–1 test and the autocorrelation function and strangeness was verified through the correlation dimension. Notably, when the data was bandpass filtered to isolate the fundamental azimuthal mode, type-II Pomeau-Manneville intermittency was observed in the azimuthal mode of an annular combustor en route to chaos. However, including the first harmonic of the fundamental mode in the data was found to obscure the low-amplitude chaos between the intermittent bursts of periodicity. This led to a different form of intermittency, one involving switching between high-amplitude periodicity and medium-amplitude combinational dynamics consisting of period-1 and period-2 limit cycles. Put together, these observations reveal that the harmonic content of the system has a profound influence on the low-amplitude pressure response, altering the intermittent dynamics during states in which the mode orientation changes.

ACKNOWLEDGMENTS

This work has received funding from the European Union's Horizon 2020 research and innovation program under Grant Agreement No. 677931 (TAIAC) and the Norwegian Research Council, Project No. 299946 (STA). Z.Y. and L.K.B.L. were supported by the Research Grants Council of Hong Kong (Projects No. 16210419 and No. 16200220).

APPENDIX

Figure 7 shows stability maps in a parameter space defined by the mass flow rate and the equivalence ratio. These maps encapsulate the various self-excited thermoacoustic modes arising at different hydrogen power fractions. The top row shows the normalized pressure amplitude, while the bottom row shows the dominant frequency of the thermoacoustic modes. The data were sampled during steady operation, after any transient features due to ramping have decayed. The data correspond to the dominant modes in terms of the amplitude of the pressure oscillations. The focus is on hydrogen power fractions in the range $P_{\mathrm{H}} = 0.3$–0.5 because the use of either lower values ($P_{\mathrm{H}} = 0.0$–0.2) or higher values ($P_{\mathrm{H}} = 0.6$–0.7) did not lead to thermoacoustic instability. These limiting conditions are omitted in the interest of brevity.

In general, as the equivalence ratio and mass flow rate increase, the mean absolute chamber pressure rises (from 136 to 232 kPa) and the bulk flow velocity decreases (from 29.7 to 22.9 ms^{-1}). For the highest mass flow rates and equivalence ratios, the system exhibits a choked boundary condition at the exit.

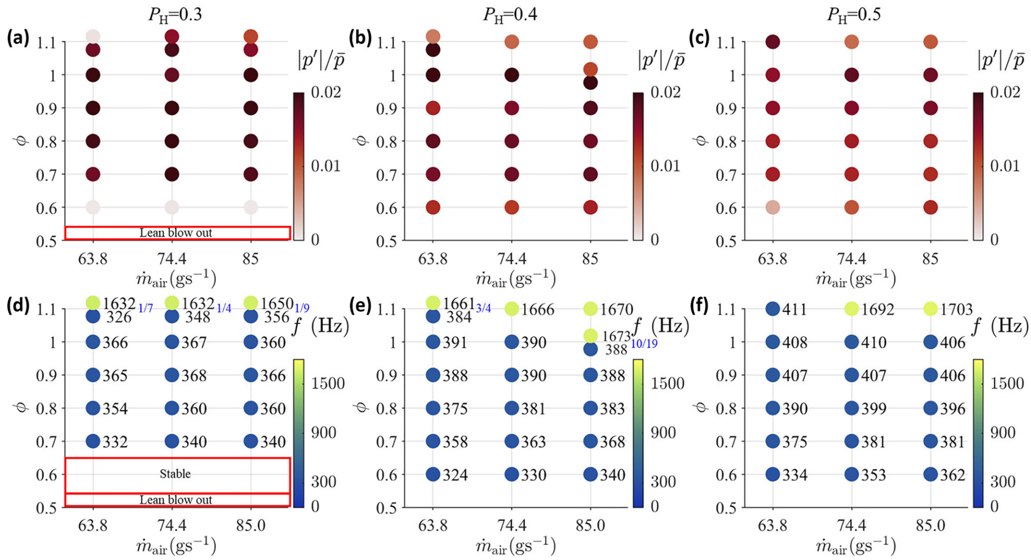

FIG. 7. Stability maps displaying the normalized pressure amplitude (a)–(c) and the dominant frequency (d)–(f) of the thermoacoustic modes for various mass flow rates and equivalence ratios. Each column corresponds to a unique hydrogen fraction: $P_H = 0.3$, 0.4, and 0.5. In the bottom row (d)–(f), the appearance of two data markers at the same operating point indicates the coexistence of two dynamical states. The blue text adjacent to these markers denotes the probability of generating azimuthal modes, expressed as N_{azi}/N_{tests} based on calculations involving at least four test runs. Specifically, the data points at $P_H = 0.3$ and $\phi = 0.6$, corresponding to air mass flow rates of $\dot{m}_{air} = 63.8$, 74.4, and 85.0 gs^{-1}, are stable states. These states are dominated by noise, exhibiting very low amplitudes, and are highlighted with a red box. Below this, lean blow out is highlighted with a separate red box. For higher hydrogen fractions than those shown, the system is stable with only low-amplitude fluctuations, so these results are not shown.

The stability boundary changes slightly with P_H, but generally the system becomes more thermoacoustically unstable as the equivalence ratio increases. At moderate values of the equivalence ratio, the system is dominated by self-excited longitudinal modes with frequencies ranging from 258 to 411 Hz and with amplitudes of up to around 2% of the mean chamber pressure. However, when $P_H = 0.4$ and 0.5, at the highest equivalence ratios and mass flow rates, the longitudinal modes are always suppressed, replaced by azimuthal modes with frequencies ranging from 1666 to 1703 Hz and amplitudes of around 1% of the mean chamber pressure. Several operating points along this boundary can support bistable behavior (denoted by dual markers in Fig. 7), where either high-amplitude azimuthal or longitudinal modes become self-excited after steady operating conditions are reached, depending on the initial conditions. When present, azimuthal modes are characterized by a single transition event—a shift from a longitudinal to an azimuthal mode. In Fig. 7, the blue fractions at the bistable operating points indicate the probability of an azimuthal mode being generated, in terms of the number of repeat measurements made at each condition.

---

[1] A. R. Masri, Challenges for turbulent combustion, Proc. Combust. Inst. **38**, 121 (2021).

[2] M. R. Bothien, A. Ciani, J. P. Wood, and G. Fruechtel, Toward decarbonized power generation with gas turbines by using sequential combustion for burning hydrogen, ASME. J. Eng. Gas Turbines Power **141**, 121013 (2019).

[3] J. Beita, M. Talibi, S. Sadasivuni, and R. Balachandran, Thermoacoustic instability considerations for high hydrogen combustion in lean premixed gas turbine combustors: A review, Hydrogen **2**, 33 (2021).

[4] D. Noble, D. Wu, B. Emerson, S. Sheppard, T. Lieuwen, and L. Angello, Assessment of current capabilities and near-term availability of hydrogen-fired gas turbines considering a low-carbon future, J. Eng. Gas Turbines Power **143**, 041002 (2021).

[5] M. Moliere, Benefiting From the wide fuel capability of gas turbines: A review of application opportunities, in *Proceedings of the ASME Turbo Expo 2002: Power for Land, Sea, and Air, Volume 1: Turbo Expo 2002, Amsterdam, The Netherlands, June 3–6, 2002* (ASME, 2002), Paper No. GT2002-30017, pp. 227–238.

[6] H. M. Altay, R. L. Speth, D. E. Hudgins, and A. F. Ghoniem, Flame-vortex interaction driven combustion dynamics in a backward-facing step combustor, Combust. Flame **156**, 1111 (2009).

[7] S. Hong, S. J. Shanbhogue, R. L. Speth, and A. F. Ghoniem, On the phase between pressure and heat release fluctuations for propane/hydrogen flames and its role in mode transitions, Combust. Flame **160**, 2827 (2013).

[8] M. C. Lee, J. Yoon, S. Joo, J. Kim, J. Hwang, and Y. Yoon, Investigation into the cause of high multi-mode combustion instability of H2/CO/CH4 syngas in a partially premixed gas turbine model combustor, Proc. Combust. Inst. **35**, 3263 (2015).

[9] B. Ahn, T. Indlekofer, J. R. Dawson, and N. A. Worth, Heat release rate response of azimuthal thermoacoustic instabilities in a pressurized annular combustor with methane/hydrogen flames, Combust. Flame **244**, 112274 (2022).

[10] N. A. Baraiya and S. R. Chakravarthy, Effect of syngas composition on high frequency combustion instability in a non-premixed turbulent combustor, Int. J. Hydrogen Energy **44**, 6299 (2019).

[11] D. W. Davis, P. L. Therkelsen, D. Littlejohn, and R. K. Cheng, Effects of hydrogen on the thermo-acoustics coupling mechanisms of low-swirl injector flames in a model gas turbine combustor, Proc. Combust. Inst. **34**, 3135 (2013).

[12] J. Zhang and A. Ratner, Experimental study on the excitation of thermoacoustic instability of hydrogen-methane/air premixed flames under atmospheric and elevated pressure conditions, Int. J. Hydrogen Energy **44**, 21324 (2019).

[13] B. Ahn, T. Indlekofer, J. R. Dawson, and N. A. Worth, Transient thermo-acoustic responses of methane/hydrogen flames in a pressurized annular combustor, ASME. J. Eng. Gas Turbines Power **144**, 011018 (2022).

[14] W. Krebs, P. Flohr, B. Prade, and S. Hoffmann, Thermoacoustic stability chart for high-intensity gas turbine combustion systems, Combust. Sci. Technol. **174**, 99 (2002).

[15] N. Noiray and B. Schuermans, On the dynamic nature of azimuthal thermoacoustic modes in annular gas turbine combustion chambers, Proc. R. Soc. A **469**, 20120535 (2013).

[16] J. R. Seume, N. Vortmeyer, W. Krause, J. Hermann, C.-C. Hantschk, P. Zangl, S. Gleis, D. Vortmeyer, and A. Orthmann, Application of active combustion instability control to a heavy duty gas turbine, J. Eng. Gas Turbines Power **120**, 721 (1998).

[17] P. Wolf, G. Staffelbach, L. Y. Gicquel, J. D. Müller, and T. Poinsot, Acoustic and large eddy simulation studies of azimuthal modes in annular combustion chambers, Combust. Flame **159**, 3398 (2012).

[18] N. A. Worth and J. R. Dawson, Modal dynamics of self-excited azimuthal instabilities in an annular combustion chamber, Combust. Flame **160**, 2476 (2013).

[19] J.-F. Bourgouin, D. Durox, J. P. Moeck, T. Schuller, and S. Candel, Self-sustained instabilities in an annular combustor coupled by azimuthal and longitudinal acoustic modes, in *Proceedings of the ASME Turbo Expo 2013: Turbine Technical Conference and Exposition. Volume 1B: Combustion, Fuels and Emissions. San Antonio, Texas, USA. June 3–7, 2013* (American Society of Mechanical Engineers, New York, 2013), p. V01BT04A007.

[20] G. Vignat, D. Durox, A. Renaud, and S. Candel, High amplitude combustion instabilities in an annular combustor inducing pressure field deformation and flame blow off, J. Eng. Gas Turbines Power **142**, 011016 (2020).

[21] N. Zettervall, N. Worth, M. Mazur, J. Dawson, and C. Fureby, Large eddy simulation of CH4-air and c2h4-air combustion in a model annular gas turbine combustor, Proc. Combust. Inst. **37**, 5223 (2019).

[22] A. Faure-Beaulieu, T. Indlekofer, J. R. Dawson, and N. Noiray, Imperfect symmetry of real annular combustors: beating thermoacoustic modes and heteroclinic orbits, J. Fluid Mech. **925**, R1 (2021).
[23] A. Roy, S. Singh, A. Nair, S. Chaudhuri, and R. I. Sujith, Flame dynamics during intermittency and secondary bifurcation to longitudinal thermoacoustic instability in a swirl-stabilized annular combustor, Proc. Combust. Inst. **38**, 6221 (2021).
[24] S. Singh, A. Roy, K. V. Reeja, A. Nair, S. Chaudhuri, and R. I. Sujith, Intermittency, secondary bifurcation and mixed-mode oscillations in a Swirl-Stabilized annular combustor: Experiments and Modeling, J. Eng. Gas Turbines Power **143**, 1 (2021).
[25] K. Prieur, D. Durox, T. Schuller, and S. Candel, A hysteresis phenomenon leading to spinning or standing azimuthal instabilities in an annular combustor, Combust. Flame **175**, 283 (2017).
[26] J.-F. Bourgouin, D. Durox, J. Moeck, T. Schuller, and S. Candel, A new pattern of instability observed in an annular combustor: The slanted mode, Proc. Combust. Inst. **35**, 3237 (2015).
[27] Y. Fang, Y. Yang, K. Hu, G. Wang, J. Li, and Y. Zheng, Experimental study on self-excited thermoacoustic instabilities and intermittent switching of azimuthal and longitudinal modes in an annular combustor, Phys. Fluids **33**, 084104 (2021).
[28] M. Mazur, Y. H. Kwah, T. Indlekofer, J. R. Dawson, and N. A. Worth, Self-excited longitudinal and azimuthal modes in a pressurised annular combustor, Proc. Combust. Inst. **38**, 5997 (2021).
[29] T. Indlekofer, B. Ahn, Y. H. Kwah, S. Wiseman, M. Mazur, J. R. Dawson, and N. A. Worth, The effect of hydrogen addition on the amplitude and harmonic response of azimuthal instabilities in a pressurized annular combustor, Combust. Flame **228**, 375 (2021).
[30] P. Knoop, F. Culick, and E. Zukoski, Extension of the stability of motions in a combustion chamber by nonlinear active control based on hysteresis, Combust. Sci. Technol. **123**, 363 (1997).
[31] T. C. Lieuwen, Experimental investigation of limit-cycle oscillations in an unstable gas turbine combustor, J. Propul. Power **18**, 61 (2002).
[32] G. Bonciolini, D. Ebi, U. Doll, M. Weilenmann, and N. Noiray, Effect of wall thermal inertia upon transient thermoacoustic dynamics of a swirl-stabilized flame, Proc. Combust. Inst. **37**, 5351 (2019).
[33] H. Gotoda, M. Amano, T. Miyano, T. Ikawa, K. Maki, and S. Tachibana, Characterization of complexities in combustion instability in a lean premixed gas-turbine model combustor, Chaos **22**, 043128 (2012).
[34] O. A. Rosso, H. A. Larrondo, M. T. Martin, A. Plastino, and M. A. Fuentes, Distinguishing noise from chaos, Phys. Rev. Lett. **99**, 154102 (2007).
[35] V. Nair and R. Sujith, Multifractality in combustion noise: predicting an impending combustion instability, J. Fluid Mech. **747**, 635 (2014).
[36] N. Noiray and B. Schuermans, Deterministic quantities characterizing noise driven Hopf bifurcations in gas turbine combustors, Int. J. Non Linear Mech. **50**, 152 (2013).
[37] D. G. Goodwin, H. K. Moffat, and R. L. Speth, Cantera: An object-oriented software toolkit for chemical kinetics, thermodynamics, and transport processes, version 2.3.0., 2017.
[38] H. T. Nygård, G. Ghirardo, and N. A. Worth, Azimuthal flame response and symmetry breaking in a forced annular combustor, Combust. Flame **233**, 111565 (2021).
[39] B. Ahn, H. T. Nygård, L. K. B. Li, and N. A. Worth, Flame dynamics in a pressurised annular combustor with simultaneous longitudinal-azimuthal thermoacoustic modes, in *14th Asia-Pacific Conference on Combustion* (2023).
[40] J. Blimbaum, M. Zanchetta, T. Akin, V. Acharya, J. O'Connor, D. Noble, and T. Lieuwen, Transverse to longitudinal acoustic coupling processes in annular combustion chambers, Int. J. Spray Combust. Dyn. **4**, 275 (2012).
[41] G. Ghirardo and M. R. Bothien, Quaternion structure of azimuthal instabilities, Phys. Rev. Fluids **3**, 113202 (2018).
[42] Y. Guan, K. Moon, K. T. Kim, and L. K. B. Li, Synchronization and chimeras in a network of four ring-coupled thermoacoustic oscillators, J. Fluid Mech. **938**, A5 (2022).
[43] M. Lee, Early warning detection of thermoacoustic instability using three-dimensional complexity-entropy causality space, Exp. Therm Fluid Sci. **130**, 110517 (2022).
[44] Y. Cao, W. wen Tung, J. B. Gao, V. A. Protopopescu, and L. M. Hively, Detecting dynamical changes in time series using the permutation entropy, Phys. Rev. E **70**, 046217 (2004).

[45] P. W. Lamberti, M. T. Martin, A. Plastino, and O. A. Rosso, Intensive entropic non-triviality measure, Physica A **334**, 119 (2004).
[46] P. Arora, Deepali, and S. Varshney, Analysis of K-Means and K-Medoids Algorithm for Big Data, Phys. Proc. **78**, 507 (2016).
[47] F. Takens, Detecting strange attractors in turbulence, in *Dynamical Systems and Turbulence, Warwick 1980* (Springer, Berlin, 2006), pp. 366–381.
[48] H. Kantz and T. Schreiber, *Nonlinear Time Series Analysis* (Cambridge University Press, Cambridge, UK, 2004), Vol. 7.
[49] A. M. Fraser and H. L. Swinney, Independent coordinates for strange attractors from mutual information, Phys. Rev. A **33**, 1134 (1986).
[50] M. B. Kennel, R. Brown, and H. D. Abarbanel, Determining embedding dimension for phase-space reconstruction using a geometrical construction, Phys. Rev. A **45**, 3403 (1992).
[51] A. Prasad, S. S. Negi, and R. Ramaswamy, Strange nonchaotic attractors, Int. J. Bifurcation Chaos Appl. Sci. Eng. **11**, 291 (2001).
[52] H. Kantz and T. Schreiber, *Nonlinear Time Series Analysis* (Cambridge University Press, Cambridge, UK, 2003), p. 388.
[53] A. S. Pikovsky, U. Feudel, and S. P. Kuznetsov, *Strange Nonchaotic Attractors* (World Scientific, Singapore, 2006), Vol. 56.
[54] D. Premraj, S. A. Pawar, L. Kabiraj, and R. I. Sujith, Strange nonchaos in self-excited singing flames, Europhys. Lett. **128**, 54005 (2019).
[55] G. A. Gottwald and I. Melbourne, A new test for chaos in deterministic systems, Proc. R. Soc. London A **460**, 603 (2004).
[56] G. A. Gottwald and I. Melbourne, On the implementation of the 0–1 test for chaos, SIAM J. Appl. Dyn. Syst. **8**, 129 (2009).
[57] B. Krese and E. Govekar, Nonlinear analysis of laser droplet generation by means of 0–1 test for chaos, Nonlinear Dyn. **67**, 2101 (2012).
[58] G. A. Gottwald and I. Melbourne, On the validity of the 0–1 test for chaos, Nonlinearity **22**, 1367 (2009).
[59] R. Gopal, A. Venkatesan, and M. Lakshmanan, Applicability of 0–1 test for strange nonchaotic attractors, Chaos **23**, 023123 (2013).
[60] B. Albrecht, H. Deutsch, R. Leven, and C. Wilke, Three-frequency quasiperiodicity and chaos in a neon glow discharge, Phys. Scr. **47**, 196 (1993).
[61] Y. Guan, M. Murugesan, and L. K. B. Li, Strange nonchaotic and chaotic attractors in a self-excited thermoacoustic oscillator subjected to external periodic forcing, Chaos **28**, 093109 (2018).
[62] G. E. Box, G. M. Jenkins, G. C. Reinsel, and G. M. Ljung, *Time Series Analysis: Forecasting and Control* (John Wiley & Sons, New York, 2015).
[63] J.-P. Eckmann, S. O. Kamphorst, and D. Ruelle, Recurrence plots of dynamical systems, EPL **4**, 973 (1987).
[64] N. Marwan, M. C. Romano, M. Thiel, and J. Kurths, Recurrence plots for the analysis of complex systems, Phys. Rep. **438**, 237 (2007).
[65] K. Klimaszewska and J. J. Żebrowski, Detection of the type of intermittency using characteristic patterns in recurrence plots, Phys. Rev. E **80**, 026214 (2009).
[66] S. A. Pawar, R. Vishnu, M. Vadivukkarasan, M. Panchagnula, and R. Sujith, Intermittency route to combustion instability in a laboratory spray combustor, J. Eng. Gas Turbines Power **138**, 041505 (2016).
[67] Y. Guan, V. Gupta, and L. K. B. Li, Intermittency route to self-excited chaotic thermoacoustic oscillations, J. Fluid Mech. **894**, R3 (2020).
[68] Y. Pomeau and P. Manneville, Intermittent transition to turbulence in dissipative dynamical systems, Commun. Math. Phys. **74**, 189 (1980).
[69] M. Mazur, H. T. Nygård, J. R. Dawson, and N. A. Worth, Characteristics of self-excited spinning azimuthal modes in an annular combustor with turbulent premixed bluff-body flames, Proc. Combust. Inst. **37**, 5129 (2019).
[70] N. Noiray, M. Bothien, and B. Schuermans, Investigation of azimuthal staging concepts in annular gas turbines, Combust. Theory Model. **15**, 585 (2011).

[71] G. Ghirardo and M. P. Juniper, Azimuthal instabilities in annular combustors: standing and spinning modes, Proc. R. Soc. A **469**, 20130232 (2013).

[72] N. A. Worth and J. R. Dawson, Effect of equivalence ratio on the modal dynamics of azimuthal combustion instabilities, Proc. Combust. Inst. **36**, 3743 (2017).

[73] P. Manneville, *Instabilities, Chaos and Turbulence*, 2nd ed. (Imperial College Press, London, UK, 2010).

[74] E. Schöll and H. G. Schuster, *Handbook of Chaos Control* (Wiley, New York, 2008).

[75] E. Ott, *Chaos in Dynamical Systems*, 2nd ed. (Cambridge University Press, Cambridge, England, 2002).

[76] J. Sacher, W. Elsässer, and E. O. Göbel, Intermittency in the coherence collapse of a semiconductor laser with external feedback, Phys. Rev. Lett. **63**, 2224 (1989).

[77] Y. Ono, K. Fukushima, and T. Yazaki, Critical behavior for the onset of type-III intermittency observed in an electronic circuit, Phys. Rev. E **52**, 4520 (1995).

[78] L. Kabiraj and R. Sujith, Nonlinear self-excited thermoacoustic oscillations: intermittency and flame blowout, J. Fluid Mech. **713**, 376 (2012).

[79] V. Nair, G. Thampi, and R. Sujith, Intermittency route to thermoacoustic instability in turbulent combustors, J. Fluid Mech. **756**, 470 (2014).

[80] R. Sujith and S. Pawar, *Thermoacoustic Instability*, Series in Synergetics (Springer, Berlin, 2021).

[81] P. Grassberger and I. Procaccia, Characterization of strange attractors, Phys. Rev. Lett. **50**, 346 (1983).

[82] H. G. Schuster and W. Just, *Deterministic Chaos*, 4th ed. (Wiley, New York, 2005).

[83] A. Arneodo, P. Coullet, and C. Tresser, Possible new strange attractors with spiral structure, Commun. Math. Phys. **79**, 573 (1981).

[84] R. Ganapathy and A. K. Sood, Intermittency route to rheochaos in wormlike micelles with flow-concentration coupling, Phys. Rev. Lett. **96**, 108301 (2006).

[85] F. Huhn and L. Magri, Stability, sensitivity and optimisation of chaotic acoustic oscillations, J. Fluid Mech. **882**, A24 (2020).

[86] T. Hachijo, S. Masuda, T. Kurosaka, and H. Gotoda, Early detection of thermoacoustic combustion oscillations using a methodology combining statistical complexity and machine learning, Chaos **29**, 103123 (2019).

[87] T. Kobayashi, S. Murayama, T. Hachijo, and H. Gotoda, Early detection of thermoacoustic combustion instability using a methodology combining complex networks and machine learning, Phys. Rev. Appl. **11**, 064034 (2019).